Effects of lithosphere on the long-wavelength gravity anomalies and their implications for the formation of the Tharsis rise on Mars

Shijie Zhong
Department of Physics, University of Colorado at Boulder, Boulder, Colorado, USA

Received 5 September 2001; revised 4 February 2002; accepted 29 March 2002; published 24 July 2002.

[1] The Tharsis rise represents the most significant long-wavelength gravity and topography anomalies on Mars. Two competing models have been proposed to explain the origin of these anomalies. In the first model the Tharsis rise is attributed to loading of volcanic construction on the lithosphere, while in the second model these anomalies are explained as dynamic effects of a one-plume thermal structure below the Tharsis rise. In this study we seek to distinguish between these two models by formulating a generalized viscoelastic loading model that determines responses to loads at different depths. With this new formulation we found that the instantaneous viscous flow loading formulation used to compute responses from a plume may significantly overestimate the geoid anomalies if the elastic thickness of the Tharsis lithosphere is ~150 km as inferred from gravity and topography data. We suggest that the one-plume structure if currently existing below the Tharsis rise may be responsible for only a small fraction (<10%) of the Tharsis geoid anomalies and that other processes, including surface loading of volcanic construction, may be the primary cause of the geoid anomalies. The plume structure is inefficient in producing geoid anomalies because the long-wavelength components of the plume structure are confined to a ~300 km layer below the lithosphere in which the geoid response is minimal. Future studies on gravity and topography at different wavelengths may put constraints on possible contribution of a plume to the elevated Tharsis topography. *INDEX TERMS:* 5417 Planetology: Solid Surface Planets: Gravitational fields (1227); 5430 Planetology: Solid Surface Planets: Interiors (8147); 5480 Planetology: Solid Surface Planets: Volcanism (8450); 8122 Tectonophysics: Dynamics, gravity and tectonics; *KEYWORDS:* Martian geophysics, Tharsis rise, geoid, mantle plumes, lithosphere

1. Introduction

[2] The gravity and topography observations show that the Tharsis rise and crustal dichotomy are the main features on the Martian surface [*Smith et al.*, 1999a, 1999b; *Hartmann*, 1973]. The topographic contrast between the southern highlands and northern lowlands defines the crustal dichotomy. Superimposed on the dichotomy is the Tharsis rise that occupies about one quarter of the Martian surface area. The Tharsis rise is characterized by successive and concentrated tectonic activity and volcanism that spans Noachian to Amazonian times [*Tanaka et al.*, 1992]. Recent studies of tectonic features in the western hemisphere with the MGS data suggest that the majority of Tharsis structural features were formed during the Noachian [*Anderson et al.*, 2001]. Flexural loading models for the Tharsis based on the MGS gravity and topography data demonstrate that most of the strain field and tectonic structures of the Noachian age in the western hemisphere can be explained as a result of the loading of Tharsis on an elastic lithosphere [*Banerdt and Golombek*, 2000]. This implies that a significant fraction of the Tharsis rise may have been formed during the Noachian [*Banerdt and Golombek*, 2000]. The long-wavelength gravity and topography anomalies are predominated by the Tharsis rise (Figure 1) [*Smith et al.*, 1999a, 1999b]. It has been suggested that much of long-wavelength gravity and topography can be explained as a consequence of loading of the Tharsis rise [*Phillips et al.*, 2001]. Therefore, the formation of the Tharsis has important implications for understanding the Martian gravity anomalies, tectonics, volcanism, and long-term thermal evolution [*Solomon and Head*, 1990].

[3] Two competing models have been proposed to explain the present-day topography and gravity of the Tharsis rise. In the first model, the Tharsis rise is formed mainly by volcanic construction and magmatic intrusion and their associated lithospheric flexure [*Solomon and Head*, 1982; *Willemann and Turcotte*, 1982; *Banerdt and Golombek*, 2000]. The simplicity of this model and its success in explaining surface observations give it a wide range of applications in studies of Mars [*Banerdt et al.*, 1992; *Phillips et al.*, 2001; *Zuber et al.*, 2000]. Implicit to this model is that the mantle contribution to the topography and gravity of the Tharsis rise is secondary. However, this model does not directly address the heat sources that are

0148-0227/02/2001JE001589$09.00

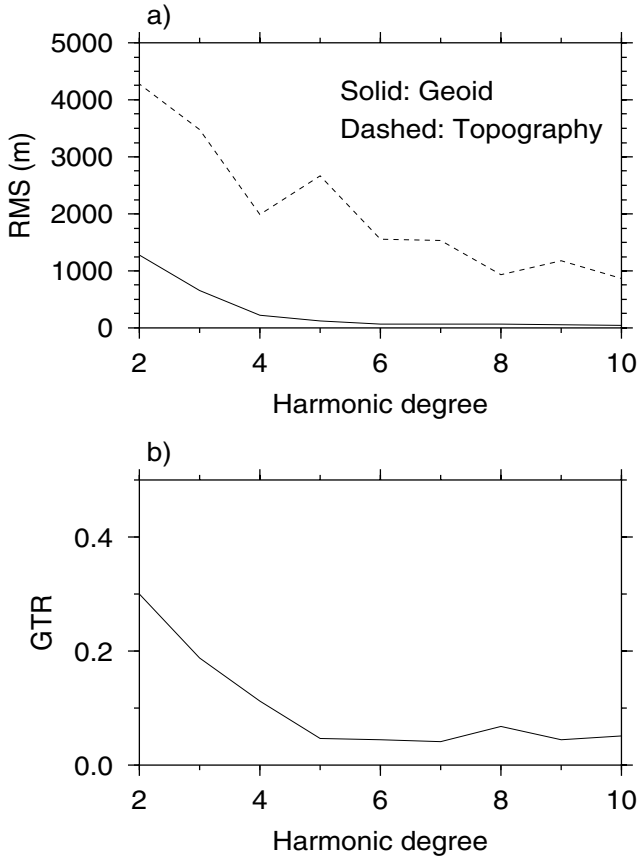

Figure 1. The RMS of the spectra of surface topography and geoid (degrees 2–10) for Mars (a) and the ratio of geoid to topography (b). The spectra are computed with spherical harmonic functions that are normalized to 1.

responsible for the formation of the volcanic construction of the Tharsis.

[4] In the second model, the gravity and topography of Tharsis are interpreted as dynamic effects of an upwelling mantle plume below the Tharsis [*Kiefer and Hager*, 1989; *Kiefer et al.*, 1996; *Harder and Christensen*, 1996; *Harder*, 2000]. The main rationale behind this idea is that long-wavelength gravity anomalies are more likely derived from the mantle and that the successive volcanism on Tharsis requires deep heat sources. This plume model has gained support from both analyses of tectonic features [*Mege and Masson*, 1996] and mantle convection simulations [*Harder and Christensen*, 1996; *Breuer et al.*, 1998; *Harder*, 2000]. Mantle convection models with an endothermic phase change (i.e., the spinel to perovskite phase change) show that a one-plume thermal structure may develop dynamically in the Martian mantle [*Harder and Christensen*, 1996]. This one-plume structure may not only provide the concentrated heat for the successive volcanism in the Tharsis region, it also produces topographic uplift and geoid anomalies that may account for the observations [*Harder*, 2000].

[5] These two competing models not only assume different loads (i.e., volcanic construction above or within the lithosphere in the flexural loading model versus the buoyancy associated with mantle plume in the one-plume model) but also use different loading formulation for computing geoid anomalies. In general, geoid anomalies may be induced by density anomalies (i.e., loads) and their induced deflections (or topography) of density boundaries, here considered to be at the surface and core-mantle boundary (CMB) [e.g., *Hager and Richards*, 1989]. In the flexural loading model, the surface deflection induced by surface loads is determined by a thin elastic shell model [*Turcotte et al.*, 1981; *Willemann and Turcotte*, 1982]. In the mantle plume models for the Tharsis, the mantle buoyancy is dynamically determined from thermal convection calculations, and the buoyancy-induced deflections at the surface and CMB are determined from an instantaneous viscous flow (IVF) formulation with a high viscosity lid simulating the lithosphere [*Kiefer et al.*, 1996; *Harder*, 2000], inherited from studies for the Earth's mantle dynamics [*Hager and Richards*, 1989].

[6] In this paper, we seek to distinguish between these two competing models for the formation of the Tharsis rise. With a newly developed viscoelastic formulation for determining deflections at the surface and CMB induced by loads at different depths, we will demonstrate that the IVF model by ignoring the effects of elastic lithosphere may significantly overestimate the geoid over an upwelling plume. The effects of elastic plates depend on the thickness of elastic plates. If the thickness of elastic plates for the Tharsis is ~150 km, as suggested by the coherence analyses of gravity and topography for relatively young tectonic features in the Tharsis region [*Zuber et al.*, 2000; *McGovern et al.*, 2000], our calculations show that contribution of the plume buoyancy to the geoid in the Tharsis region is rather small. This suggests that the geoid anomalies in the Tharsis region may be caused mainly by loads above and/or within the lithosphere.

[7] In what follows, first we will present a viscoelastic formulation for determining boundary deflections induced by loads at different depths. Second, we will study general characteristics of loading for viscoelastic media and show that the IVF model and the elastic thin shell model are special cases of our viscoelastic formulation. Third, we will demonstrate the important difference in predicting surface deflections and the geoid anomalies between the viscoelastic and IVF models when they are applied to the Tharsis loading problem. The implications for the formation of the Tharsis are given in final section on discussions and conclusions.

2. A Model for Response of Viscoelastic Media to Surface and Internal Loads

[8] We have recently extended our previous formulation for viscoelastic loading [*Zhong*, 1997; *Zhong and Zuber*, 2000] to include internal loads in the mantle. The formulation can be briefly described as follows.

[9] The response of a self-gravitating and incompressible planet to surface and internal loads can be described by the governing equations of mass and momentum and the equation of gravitational perturbation:

$$u_{i,i} = 0, \tag{1}$$

$$\sigma_{ij,j} + \rho_0 \Phi_{,i} - \Delta\rho g \delta_{ir} = 0, \quad (2)$$

$$\Phi_{,ii} = 4\pi G \Delta\rho, \quad (3)$$

where u_i is the velocity; σ_{ij} is the stress tensor; ρ_0 is a reference density; Φ is the perturbation of gravitational potential; g is the gravity acceleration which is a function of radius; $\Delta\rho$ is the density perturbation that may represent either internal or surface loads, G is the gravitational constant, δ_{ir} is the Kronecker delta, which equals 1 when $i = r$ and 0 otherwise, $A_{,i}$ represents the spatial derivative of A with respect to coordinate x_i, and repeated indices indicate a summation.

[10] The rheological equation for an incompressible viscoelastic medium (i.e., Maxwell body) can be written as

$$\sigma_{ij} + (\eta/\mu)\dot{\sigma}_{ij} = -P\delta_{ij} + 2\eta\dot{\varepsilon}_{ij}, \quad (4)$$

where μ and η are the shear modulus and viscosity, respectively; P is the pressure; ε is the strain tensor; and the dot over the strain and stress tensors denotes the time derivative.

[11] When a surface or internal load is applied to a planet with a viscoelastic rheology, the response (i.e., the resulting deflection at the surface and CMB) can be determined by solving equations (1) – (4). Our analyses are performed in a spherical harmonic domain. We use a Laplacian transform and a propagator matrix method to first obtain solutions of the responses in the Laplacian domain (i.e., characteristic times and their corresponding eigen-functions) and then use an inverse Laplacian transform to retrieve the solutions in the time domain [*Zhong*, 1997; *Zhong and Zuber*, 2000].

[12] The post-glacial rebound is a classic geophysical problem that uses viscoelastic stress relaxation [e.g., *Cathles*, 1975; *Peltier*, 1976]. While the postglacial rebound studies use a Lagrangian formulation [e.g., *Peltier*, 1976], we employ a mixed Lagrangian and Eulerian formulation (i.e., equations 1–4). In the Lagrangian formulation for the postglacial rebound studies, a correspondence principle is often used. However, we have verified that our formulation is equivalent to those from the Lagrangian formulation by comparing with solutions from *Han and Wahr* [1995].

[13] The viscoelastic response is in general time-dependent. For density and viscoelastic structures of a planetary mantle that do not vary with time, the response asymptotically approaches a steady state value. The time-dependence is controlled by characteristic times that depend only on density and viscoelastic structures of a planetary mantle and wavelengths of loads [e.g., *Zhong and Zuber*, 2000]. For a load with a step-function loading history (i.e., the load is applied at $t = 0$ and remains the same for $t > 0$), the initial response at $t = 0$ is purely elastic but the subsequent evolution of the response is determined by viscoelastic relaxation. The response H (e.g., either the surface or CMB topography) for harmonic degree l at time t can be expressed as

$$H(l,t) = h_0(l) + \sum_{i=1}^{N} h_i(l)\exp[-t/\tau_i(l)], \quad (5)$$

where $\tau_i(l)$ and $h_i(l)$ are the characteristic time and its corresponding eigen-function, respectively, N is the number of characteristic times and is determined by the number of density and viscosity interfaces [e.g., *Han and Wahr*, 1995], and $h_0(l)$ is the steady state response. While the time-dependence is important in post-glacial rebound studies, in this study we are more interested in the steady state solutions that are important for long-term loading problems.

[14] A simplified formulation for loading problems only considers a viscous rheology and ignores the elasticity of planetary mantle and lithosphere. The rheology is given by

$$\sigma_{ij} = -P\delta_{ij} + 2\eta\dot{\varepsilon}_{ij}. \quad (6)$$

This rheology can be viewed a special case of (4) by assuming shear modulus μ to be infinite. In this formulation, one may obtain a time-dependent and steady state response by solving equations (1)–(3) and (6) (e.g., for analyses in a Cartesian geometry, see *Grimm and Solomon* [1988] and *Zhong et al.* [1996]). The time dependent response is controlled by viscous relaxation. The response can be expressed in a similar form as in (5), but the number of characteristic times N now is equal to the number of density interfaces [e.g., *Han and Wahr*, 1995] (e.g., $N = 2$ if only the surface and CMB are included in a model).

[15] An important special form of this viscous formulation is the so-called instantaneous viscous flow (IVF) formulation in which one may directly obtain the steady state viscous response by solving these equations without actually considering the time dependence. This IVF loading formulation was originally developed to study the long-wavelength gravity field for the Earth [*Hager and Richards*, 1989]. The IVF formulation has also been used to relate mantle plume buoyancy to the topography and gravity anomalies for the Tharsis [*Kiefer et al.*, 1996; *Harder and Christensen*, 1996; *Harder*, 2000].

[16] A thin elastic shell formulation, another widely used loading formulation, considers surface loads on a planetary lithosphere that is modeled as a thin elastic shell [*Brotchie and Silvester*, 1969; *Turcotte et al.*, 1981]. However, this elastic shell formulation does not account for internal loads and the response at the CMB. Compared with the viscous flow [e.g., *Harder*, 2000] and thin elastic shell formulations [e.g., *Turcotte et al.*, 1981], our viscoelastic loading formulation has important advantages: 1) Either the viscous flow formulations or the elastic flexural formulation can be considered as a special case of our viscoelastic formulation. 2) It allows us to consider planetary response to internal loads with viscous mantle but elastic lithosphere. 3) When degenerated to the limit of elastic plate, our formulation automatically includes the variations of vertical stresses that are excluded in the elastic plate formulation because of its thin plate approximation. This effect can be quite important when we deal with regional scale loads on a relatively thick plate ($\sim$100 km) [*Zhong and Zuber*, 2000].

3. Results

[17] In this section, we will first study the general characteristics of viscoelastic and viscous relaxation. Second, we will compare our viscoelastic formulation with the instantaneous viscous flow (IVF) formulation [e.g., *Harder*, 2000] and thin elastic shell formulations [*Turcotte et al.*, 1981]. Third, we will present solutions of viscoelastic response and

Table 1. Model Parameters

Parameter	Value
Parameters Relevant to the Loading Problems	
Planetary radius	3400 km
Core radius	1450 km
Shear modulus	7×10^{10} Pa
Mantle density	3400 kg m^{-3}
Core density	7000 kg m^{-3}
Gravitational acceleration	3.73 m s^{-2}
Mantle viscosity	10^{21} Pa.s
Additional Parameters for the Thermal Convection Model	
Temperature difference	1500 K
Core radius	1400 km
Lithospheric thickness	150 km
Thermal diffusivity	10^{-6} m^2 s^{-1}
Lithospheric viscosity	10^{27} Pa.s
Thermal expansivity	3×10^{-5} K^{-1}
Volumetric heating rate	8.6×10^{-9} W m^{-3}
Phase change	
Radial position	1520 km
Clapeyron slope	-3×10^6 Pa K^{-1}
Density change	210 kg m^{-3}
Half-width	30 km

compare them with those from the IVF formulation for different lithospheric thickness to demonstrate the potential drawbacks of the IVF formulation. Fourth, we will show the distribution of thermal buoyancy associated with a one-plume structure and we will argue on the basis of our viscoelastic loading models that such one-plume structure cannot account for the Tharsis gravity anomalies.

3.1. General Characteristics of Viscoelastic and Viscous Relaxation

[18] For an isoviscous mantle with a unit degree-2 load that is applied at 680-km depth with a step-function in time (Table 1 for model parameters), both viscoelastic and viscous relaxation models have two characteristic times (Table 2). The characteristic times are only dependent on mechanical structure and harmonic degree and are independent of the location or magnitude of the load [e.g., *Zhong*, 1997]. For the viscoelastic model, there is an initial elastic response in surface topography, and the topography increases with time and reaches a steady state response h_0 at time-scales controlled by the characteristic times ($\sim 10^4$ years for mantle viscosity of 10^{21} Pa.s) (Figure 2a and Table 2). For the viscous model, while the steady state topography h_0 is identical to that for the viscoelastic model, the time dependence of surface topography is different with a zero initial response (Figure 2a and Table 2). These results indicate that the shear modulus does not affect the steady state response, while it affects the transient response.

[19] However, both the transient and steady state responses are influenced by relative viscosity structure. When the top 100 km of the mantle is 1000 times more viscous than the underlying mantle, the number of characteristic times is increased to 4 for the viscoelastic model, but it remains to be 2 for the viscous model. As indicated by the characteristic times and their corresponding eigen-functions for this layered viscosity model (Table 2), compared with the isoviscous models (Figure 2a), it takes longer ($\sim 10^6$ years) for viscoelastic and viscous models to reach the steady state response and the steady state response has a larger amplitude (Figure 2b). The larger amplitude for the steady state response results from a stronger coupling of the load to the surface for a stiffer surface layer [*Hager and Richards*, 1989; *Zhong and Davies*, 1999].

[20] Increasing the viscosity for the top layer by another factor of 1000 results in even longer time to reach the steady state response ($\sim 10^9$ year in Table 2 and Figure 2c). Again the steady state responses are identical for viscoelastic and viscous models (Table 2). The eigen-functions for the viscous model indicate that the time evolution is entirely controlled by the longer characteristic time (Table 2). However, for the viscoelastic model the mode with longest characteristic time only contributes ~16% to the steady state response, and the other modes with much shorter characteristic times contribute ~84% of the steady state response (Figure 2c and Table 2). While the longest characteristic time is controlled by the large viscosity in the top layer, the short characteristic times ($<10^5$ years) are primarily controlled by the mantle viscosity and are rather insensitive to the top layer viscosity. Because of the large

Table 2. Viscoelastic Versus Viscous Relaxation at Degree 2

Viscoelastic		Viscous	
τ_i (yr)	h_i	τ_i (yr)	h_i
η_u/η_l=1			
3.56277E+03[a]	−6.45745E−01	3.10978E+03	−7.39810E−01
1.64640E+04	−5.64591E−02	1.60110E+04	−5.80564E−02
	h_0 = 7.97866E−01		h_0 = 7.97866E−01
η_u/η_l=10^3			
2.71645E+03	−3.71424E−01	1.55311E+04	−1.04896E−02
3.91212E+03	−1.40647E−01	1.07517E+05	−8.86325E−01
2.05656E+04	−1.23454E−01		
5.54315E+05	−1.65626E−01		
	h_0 = 8.96814E−01		h_0 = 8.96814E−01
η_u/η_l=10^6			
2.72225E+03	−3.75397E−01	1.60988E+04	−4.68664E−06
3.93197E+03	−1.37340E−01	1.00035E+08	−8.97812E−01
2.06530E+04	−1.27022E−01		
5.53026E+08	−1.62395E−01		
	h_0 = 8.97816E−01		h_0 = 8.97816E−01

[a]Read 3.56277E+03 as 3.56277×10^3.

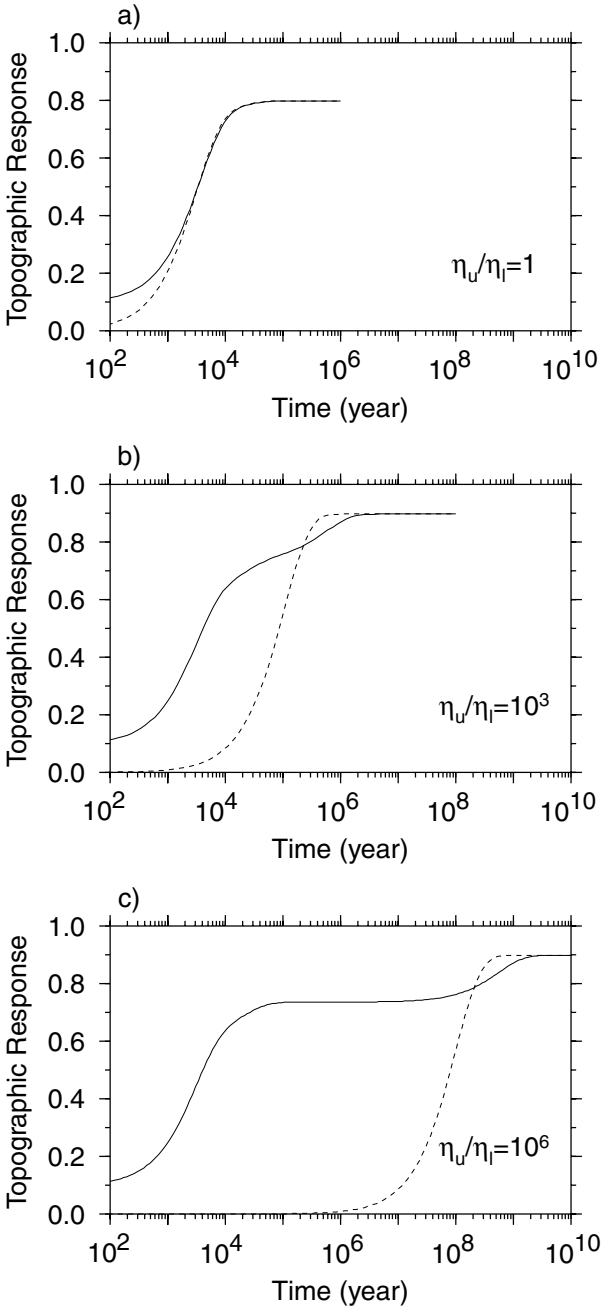

Figure 2. Time-dependent response in surface topography induced by a unit degree-2 load at a depth of 680 km with a step-function loading function from viscoelastic (solid lines) and viscous (dashed lines) models for three cases with different viscosity for the top 100 km layer: $\eta_u = \eta_l$ (a), $\eta_u = 10^3\eta_l$ (b), and $\eta_u = 10^6\eta_l$ (c).

difference between the longest and other characteristic times for the viscoelastic model, the response is nearly constant (~86% of the steady state value) from 10^5 to 10^8 years before reaching the steady state (Figure 2c).

[21] The top thermal boundary of a planetary mantle forms lithosphere with very large viscosity, because of its relatively small temperature and the temperature-dependence of viscosity. This lithospheric viscosity makes the mode with longest characteristic time observationally irrelevant. That is, the steady state response cannot be reached in geologically relevant timescales (~10^9 years). The meaningful response h_r is that associated with the viscoelastic modes with relatively short characteristic times that are insensitive to the lithospheric viscosity, or $h_r = h_0$-h_{Lg}, where h_{Lg} is the eigen-function associated with the longest characteristic time.

[22] These results have implications for other loading models including the instantaneous viscous flow (IVF) [*Hager and Richards*, 1989; *Harder*, 2000] and thin elastic shell [*Turcotte et al.*, 1981] models. For surface loads, the thin elastic shell model gives very accurate solutions for h_r, especially at long-wavelengths, as we will discuss in the next section. However, the IVF model may significantly overestimate h_r, because the IVF model solves for the steady state response h_0. When applied to the Earth [e.g., *Hager and Richards*, 1989], the IVF model may not present any problem because h_{Lg} is insignificant for the Earth with a relatively large radius and small lithospheric thickness. However, for Mars with relatively small radius and large lithospheric thickness (e.g., the inferred elastic thickness based on young surface features is >150 km [*Zuber et al.*, 2000; *McGovern et al.*, 2000], which may represent better the present-day elastic thickness), h_0 from the IVF model is significantly larger than h_r (Figure 2c), and its effects on the geoid are even larger as we will discuss later.

3.2. Viscoelastic Model Versus Thin Elastic Plate Model

[23] For surface loading in a simple two-layer viscoelastic model, if the top layer is significantly more viscous than the bottom layer, then the relevant long-term response h_r at the surface should be the same as that from an elastic shell model in which the shell thickness is the same as that for the top layer in the viscoelastic model. This is because the weak bottom layer with relatively rapid stress relaxation behaves like an inviscid flow that is incapable of supporting stresses over large timescales. The surface load is fully supported by the more viscous top layer after stress relaxation associated with the weak bottom layer is completed. This can be demonstrated by comparing the viscoelastic with thin elastic plate models for surface loading problems.

[24] The response of an elastic plate to surface loading at different harmonic degrees can be obtained from the thin elastic shell formulation by *Turcotte et al.* [1981]. We have computed the response of 50-km and 100-km thick elastic plates to surface loads from degrees 2 to 20 (Figure 3). We have also computed the responses h_r from the two-layer viscoelastic model in which the top layer with a thickness of 50 km and 100 km is significantly more viscous than the bottom layer (by 9 orders of magnitude) (Figure 3). The viscoelastic model with a thickness of 50 km for the top layer agrees excellently with the elastic shell model with a shell thickness of 50 km. However, noticeable differences exist at relatively short wavelengths between these two models for the top layer with a thickness of 100 km, and the response at degree 20 from the thin shell model is 10% smaller than that from the viscoelastic model (Figure 3b). We believe that the difference is caused by the neglect of vertical stress variations in the thin elastic shell model. The effects of vertical stress variations on the loading response increase as the ratio of elastic plate thickness to loading

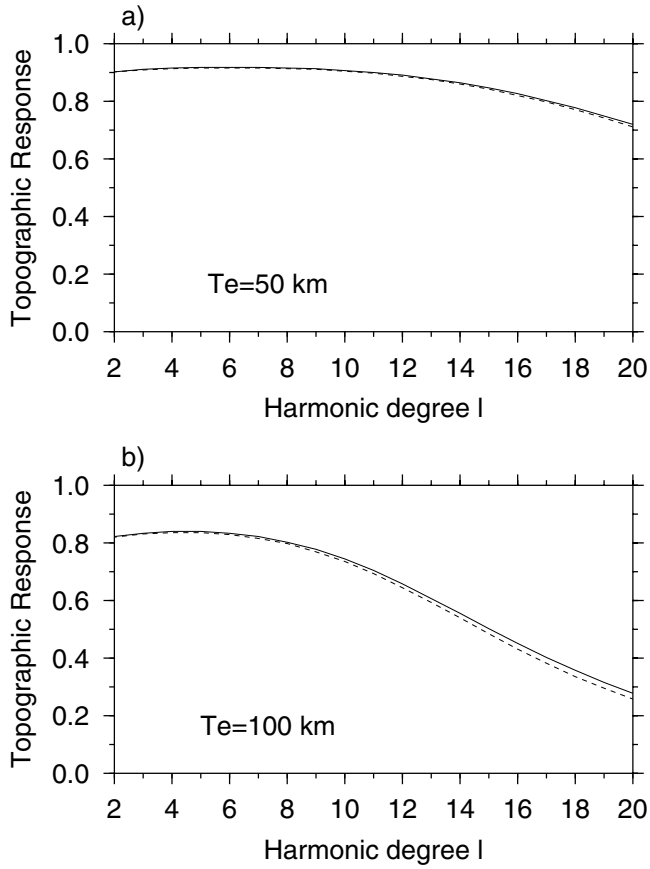

Figure 3. Comparison of the response in surface topography between the viscoelastic (solid lines) and thin elastic shell (dashed lines) models for 50-km and 100-km thick lithosphere. The viscoelastic model includes two layers: lithosphere and the mantle. The lithospheric viscosity is nine orders of magnitude higher than mantle viscosity, and the response is h_r.

wavelengths increases. Nevertheless, on the basis of these calculations we may conclude that for surface loading problems the response from the thin elastic shell model agrees well with h_r from the two-layer viscoelastic model especially at long-wavelengths. However, it is not obvious how the thin elastic shell model can be used to study the internal loading problems.

3.3. Response From Viscoelastic and IVF Models

3.3.1. Models with a 150-km-thick elastic plate

[25] We have demonstrated in section 3.1 that the response from the more realistic viscoelastic model is h_r while the response from the IVF model is h_0. In this section, we will focus on how the difference in response between the viscoelastic and IVF models (i.e., h_r and h_0) affects gravity anomalies. We will consider elastic thickness of 150 km because it was inferred from studies of gravity and topography for the Tharsis region [*Zuber et al.*, 2000; *McGovern et al.*, 2000]. For both viscoelastic and IVF models, the viscosity structure is the same with a very large viscosity for the top 150-km layer (Table 1).

[26] Following the standard practice in the studies of Earth's response [e.g., *Hager and Richards*, 1989], we compute response kernels of surface topography, CMB topography, and geoid from viscoelastic [e.g., *Zhong and Zuber*, 2000] and IVF models (Figure 4). The kernels are shown as a function of radius. Interpretation of the kernels may need some explanations, and we use the surface topography kernel (Figure 4a) as an example. The surface topography response for a given radius and harmonic degree in Figure 4a is the topography produced by a unit load at that harmonic degree with a delta function at that radius. In the previous two sections, we have shown the response to such loads in the mantle (Figure 2) and at the surface (Figure 3). In general, the closer a load to the surface (CMB), the larger topography the load produces at the surface (CMB). For the IVF model, a load at the surface is fully compensated with the kernel value of 1 (i.e., the mass anomaly for the surface topography produced by the load completely offsets the load) (Figure 4a and *Hager and Richards* [1989]). However, for the viscoelastic model with lithospheric thickness of 150 km a surface load even at degree 2 is under-compensated by surface topography with the kernel less than 0.8 (Figure 4a). The difference in the response between these two models is significant for loads at different wavelengths and radial locations throughout the mantle (Figure 4a). However, the response for the CMB topography from the viscoelastic and IVF models is rather similar, except for degree 2 at relatively shallow depths (Figure 4b). It is worthwhile to point out that the degree-2 kernel is slightly greater than 1 at shallow depths (Figure 4a). This is caused by the self-gravitation.

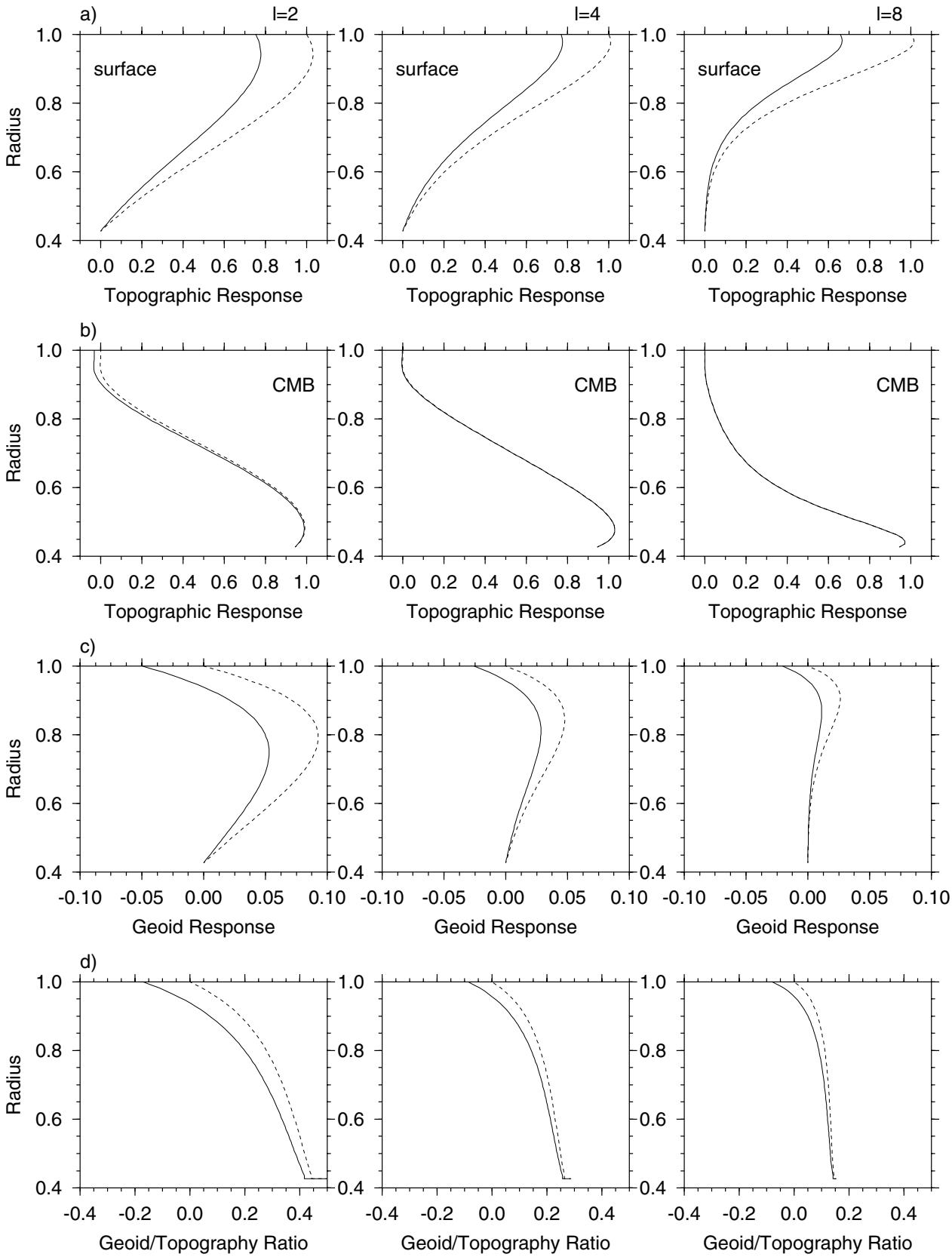

Figure 4. Comparison of the responses between the two-layer viscoelastic (solid lines) and IVF (dashed lines) models with 150-km thick lithosphere. Shown are responses in surface topography (a), CMB topography (b), the geoid (c), and the ratio of geoid to topography (d) for degrees 2 (left column), 4 (middle column) and 8 (right column). The viscoelastic and IVF models have the same viscosity structure in the mantle and lithosphere.

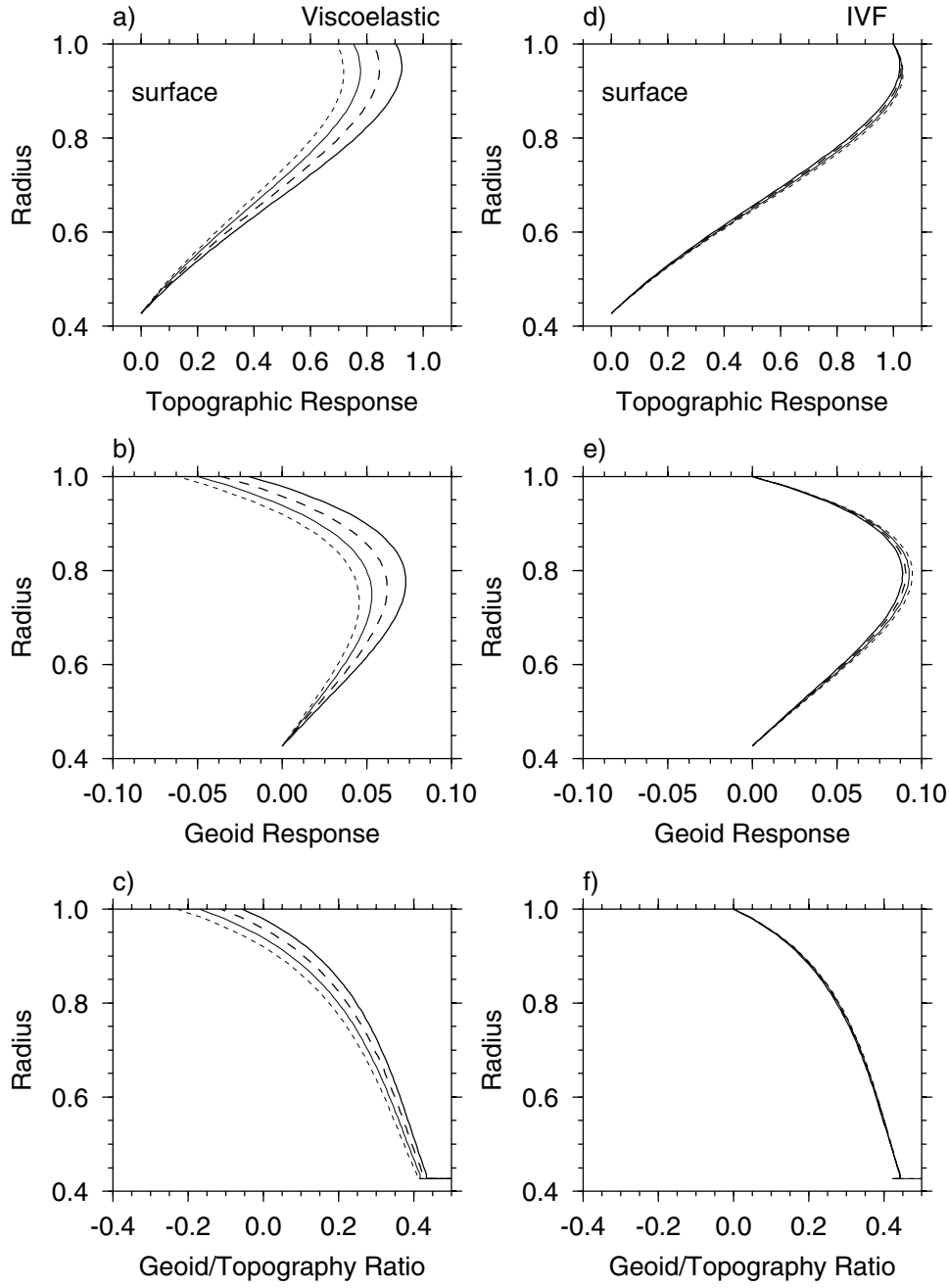

Figure 5. The effects of lithospheric thickness on the responses for two-layer viscoelastic (left column) and IVF (right column) models. Shown are the degree-2 responses in surface topography (the first row), the geoid (the second row), and the ratio of geoid to topography (the third row) for 50-km (thick solid lines), 100-km (thick dashed lines), 150-km (thin solid lines) and 200-km (thin dashed lines) thick lithosphere.

[27] The differences in responses for surface and CMB topography between the viscoelastic and IVF models have significant effects on the geoid response (Figure 4c). For the IVF model, loads near the surface produce nearly zero geoid because they are completely compensated by the surface topography induced by the loads [e.g., *Hager and Richards*, 1989]. Degree-2 loads at a depth of ~680 km (i.e., r = 0.8) produce the largest geoid anomalies (Figure 4c). However, for the viscoelastic model, surface loads produce significant negative geoid (negative geoid arises because the loads in the kernel calculations are buoyant and represent mass deficits), and buoyant internal loads immediately below the lithosphere (i.e., at radius ~0.95) produce zero geoid. Maximum positive geoid occurs at similar depths from the viscoelastic and IVF models, but the amplitude of the geoid from the viscoelastic model is significantly reduced compared with that from the IVF model (Figure 4c).

[28] It is also interesting to examine the difference for the ratio of geoid to topography (GTR) between the viscoelastic and IVF models. For the IVF models, GTR is zero at the

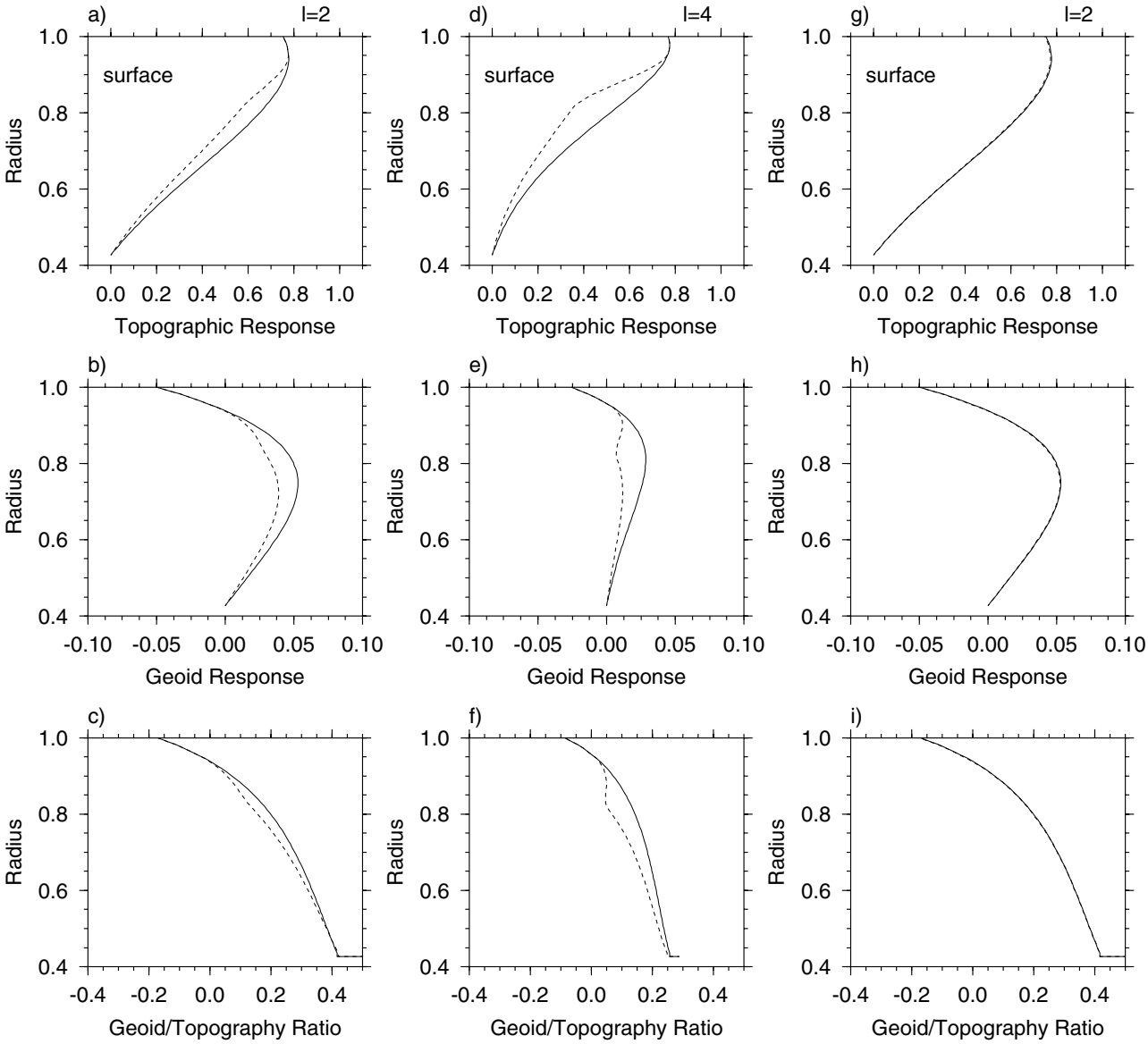

Figure 6. The effects of a weak layer below lithosphere on the surface topography (a and d in the first row), the geoid (b and e in the second row), and the ratio of geoid to topography (c and f in the third row) for degrees 2 (left column) and 4 (middle column) from viscoelastic models for 150-km thick lithosphere. Dashed and solid lines are for the case with and without a weak layer, respectively. Also shown are the degree-2 responses of surface topography (g), geoid (h), and the ratio of geoid to topography (i) from the viscoelastic formulation (solid lines) and a hybrid formulation (dashed lines).

surface and increases with depth. At a depth of ~400 km, GTR for degrees 2 and 4 is about 0.2 and 0.1, respectively (Figure 4d). For the viscoelastic models, GTR is negative throughout the lithosphere and is zero immediately below the lithosphere. GTR from the viscoelastic models within a 300-km depth range below the lithosphere is much smaller than that from the IVF model (Figure 4d). These results about the geoid and GTR have important implications for the geoid from the IVF loading formulation used by *Harder* [2000], as we will discuss later.

3.3.2. Effects of elastic thickness and mantle viscosity structure

[29] Although present-day elastic thickness for Mars is suggested to be greater than 150 km [*Zuber et al.*, 2000; *McGovern et al.*, 2000], it is interesting to examine the effects of elastic thickness on the viscoelastic and IVF loading models. In addition to calculations for 150-km lithospheric thickness, we have computed the kernels for 50 km, 100 km and 200 km lithospheric thickness. We will only show results for degree 2, because they are representative for other wavelengths.

[30] For the viscoelastic model, because a thicker lithosphere supports more elastic stress, the thicker a lithosphere, the smaller the response of the surface topography (Figure 5a). This results in a smaller geoid response and GTR at large depths and more negative geoid and GTR at shallow depths (Figures 5b and 5c). The kernels for the IVF model are not very sensitive to the lithospheric thickness.

However, the effects of lithospheric thickness on the topography and geoid responses in the IVF model are opposite to those in the viscoelastic model (Figure 5). The thicker a lithosphere, the larger the geoid and topography responses are in the IVF model (Figures 5d and 5e).

[31] We now examine the effects of mantle viscosity structure. The pressure-dependence of viscosity and partial melting may result in smaller viscosity at shallow depths below the lithosphere [e.g., *Turcotte and Schubert*, 1982; *Zhong and Zuber*, 2001]. This type of viscosity structure may also be expected from the one-plume thermal convection model, because as the plume spreads out below the lithosphere the hot flow may result in small viscosity at these depths [*Harder*, 2000]. We have computed the kernels from a viscoelastic loading formulation for a case that is identical to that in Figure 4 except that this case has a 600-km thick weak layer below the 150-km thick lithosphere. The viscosity for this weak layer is 10 times smaller than the mantle below. The weak layer results in reduction in the responses of surface topography and geoid and GTR, compared with the case without a weak layer (Figures 6a–6f for degrees 2 and 4).

3.3.3. A hybrid loading model with the IVF and thin elastic shell models

[32] We have demonstrated that the viscoelastic and IVF formulations predict different topography and geoid for surface and internal loading (Figure 4) and that the viscoelastic and elastic thin shell models yield similar response for surface loading (Figure 3). It is interesting to examine whether we can combine the IVF and elastic thin shell models (i.e., a hybrid loading model) to mimic the viscoelastic model. In this hybrid model, the kernel for surface topography is obtained by multiplying the kernel for surface topography from the IVF model with the response from the elastic shell model with the same lithospheric thickness. The geoid kernel can then be computed from this modified surface topography kernel and CMB topography kernel from the IVF model. We have found that the geoid and surface topography kernels from the hybrid model compare well with those from the viscoelastic model (Figures 6g–6i for degree 2). This suggests that under some circumstances the viscoelastic responses can be simulated with this hybrid loading model. However, this hybrid model has limitations compared with the more generalized viscoelastic loading model. The hybrid model may have difficulties in accurately predicting the transient response associated with the stress relaxation in the mantle and the lower part of lithosphere, responses from models that include lithosphere with embedded weak layers (e.g., weak lower crust), and the topography and gravity anomalies at the CMB.

3.4. Geoid and Topography From One-Plume Models

[33] In this section, we will apply the viscoelastic and IVF loading formulations to the one-plume thermal structure produced from thermal convection models with a phase change to examine to what extent the one-plume thermal model can explain the observed geoid and topography over the Tharsis and how these two loading formulations differ in predicting the geoid.

3.4.1. One-plume thermal convection model

[34] It has been suggested that one-plume thermal structure can be dynamically generated from thermal convection

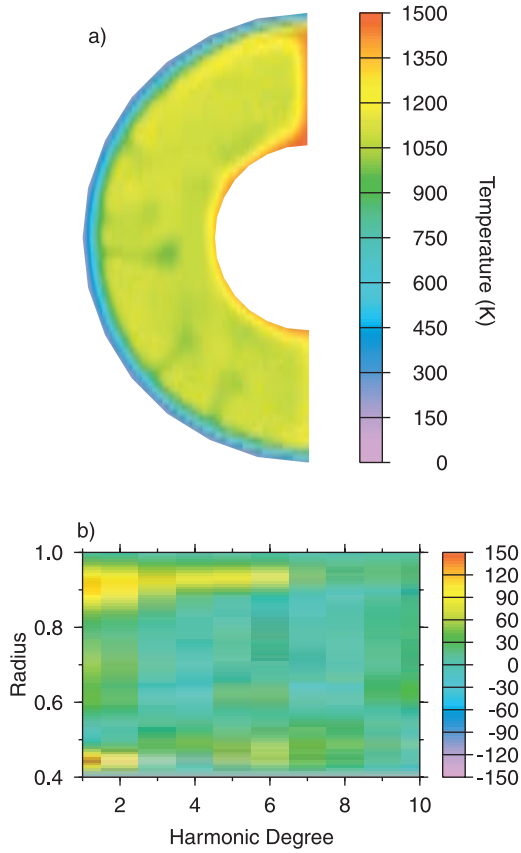

Figure 7. The differential temperature with respect to the surface for one-plume thermal structure from a spherically axisymmetric model of thermal convection with an endothermic phase change (a) and the dependence of the spectrum of the thermal structure on depth (b).

with a phase change in the Martian mantle and that such one-plume structure can explain the successive occurrence of volcanisms in the Tharsis region [*Harder and Christensen*, 1996; *Breuer et al.*, 1998; *Harder*, 2000]. While *Harder and Christensen* [1996] used an endothermic phase change corresponding to the spinel to post-spinel phase change within Earth's mantle, *Breuer et al.* [1998] employed an exothermic phase change for the olivine to spinel at a shallower depth. The advantage in using the exothermic phase change is that the model does not depend so much on the currently poorly constrained size for the metallic core (the endothermic phase change may not exist if the core is sufficiently large). However, *Harder* [2000] indicated that the one-plume structure from *Breuer et al.* [1998] resulted from an unreasonable assumption for the lithospheric viscosity rather than the exothermic phase change.

[35] We have formulated spherically axisymmetric thermal convection models [e.g., *Kellogg and King*, 1993; *Zhong and Zuber*, 2001] with an endothermic phase change using a method similar to *Christensen and Yuen* [1985] and *Zhong and Gurnis* [1994]. We use model parameters that are similar to those in *Harder* [2000] except the thickness of lithosphere (i.e., high viscosity layer) that is 150 km in our model in accord to the studies by *Zuber et al.* [2000] and

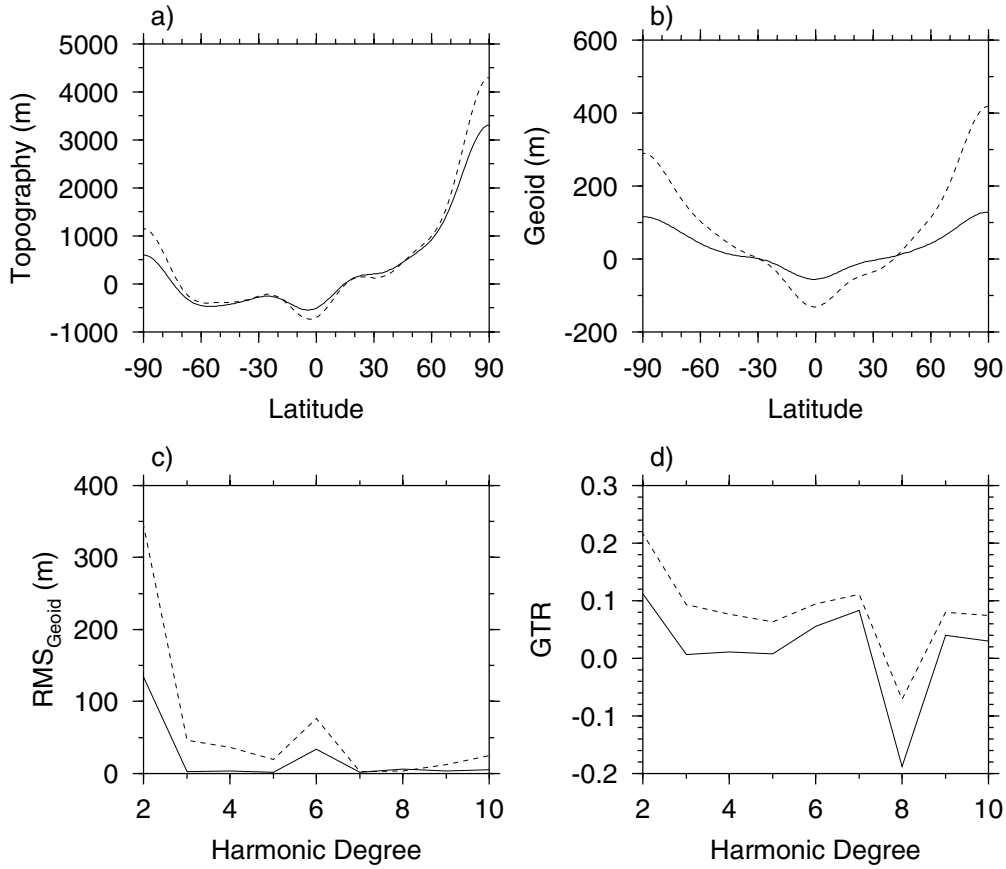

Figure 8. The dependence of surface topography (a) and geoid (b) on latitude and the dependence of the RMS of the geoid (c) and the ratio of geoid to topography on spherical harmonic degree (d) predicted from the viscoelastic (solid lines) and IVF (dashed lines) formulations for the one-plume structure in Figure 7a.

McGovern et al. [2000] but is 220 km in *Harder's* [2000] model (Table 1). Although our model is axisymmetric, it reproduces the one-plume thermal structure in Harder's models reasonably well (Figure 7a).

3.4.2. Geoid and topography induced by the one-plume thermal structure

[36] *Harder* [2000] and *Harder and Christensen* [1996] used the IVF loading formulation to compute the geoid and topography induced by the one-plume thermal structure. We will determine the plume-induced geoid and topography from the viscoelastic formulation and compare them with those from the IVF formulation. The loading models use the same viscosity structure as in the thermal convection calculations. Because only long-term responses are relevant here and because the one-plume structure is rather stable [e.g., *Harder and Christensen*, 1996], the viscoelastic formulation with a step-function loading to determine the steady state responses (i.e., h_r) is justified.

[37] Before computing the geoid and topography, we will examine how the power spectrum of the one-plume structure (e.g., Figure 7a) distributes in the mantle. The long-wavelength structure is primarily confined within a depth range of 250∼300 km near the CMB and below the lithosphere (Figure 7b). The long-wavelength structure below the lithosphere is generated as the thermal plume spreads out below the lithosphere (Figure 7a). The 250∼300 km depth range is related to the thickness of the thermal boundary layer.

[38] This spectrum distribution (Figure 7b) and the kernels for surface topography and geoid for a 150-km thick lithosphere (Figures 4a and 4c) suggest that the long-wavelength structure below the lithosphere contribute the most to the surface topography and geoid anomalies above the plume. The structure near the CMB is largely compensated at the CMB and does not produce topography and geoid anomalies at the surface (Figure 4b). It is important to notice that over the ∼300 km depth range below the lithosphere, the geoid kernels differ significantly between the viscoelastic and IVF formulations and the response for the geoid and GTR from the viscoelastic formulation are ∼4 times smaller than those from the IVF formulation (Figures 4c and 4d).

[39] The geoid and surface topography show that while the surface topography from the viscoelastic formulation is ∼20% smaller than that from the IVF formulation, the long-wavelength geoid from the viscoelastic model is ∼4 times smaller (Figures 8a and 8b). The reduction for the geoid occurs at all wavelengths especially at degrees 3 and 4 (Figure 8c) and the long-wavelength geoid is more than ten times smaller than the observed (Figure 1). GTR at degrees 2–4 from the viscoelastic formulation is significantly smaller than the observed especially at degrees 3 and 4

(Figures 8d and 1). Although the GTR at degree 8 is rather large, the magnitudes of the geoid and topography are rather small (Figure 8d).

4. Discussions

[40] The formation of the Tharsis rise has important implications for the evolution of Mars [e.g., *Solomon and Head*, 1990]. Among various models for the formation of the Tharsis, the one-plume model by *Harder and Christensen* [1996] and *Harder* [2000] provides a reasonable explanation for the successive and concentrated volcanisms in the Tharsis region. However, it is unclear how much the plume structure if it exists below the Tharsis rise contributes to the elevated topography and gravity anomalies. While *Harder* [2000] suggested that more than half of the geoid anomalies may be explained with the plume structure, our studies indicate that the geoid anomalies of *Harder* [2000] may have been significantly overestimated by as much as a factor of 4, if elastic thickness for Mars is ~150 km as suggested by *Zuber et al.* [2000] and *McGovern et al.* [2000] (Figures 4 and 8). Considering the predicted geoid anomalies from the one-plume structure by *Harder* [2000] and our calculations (Figures 8b and 8c) and the effects of a 150-km thick elastic plate (i.e., a factor of ~3 to 4 reduction for the geoid compared with the IVF load models in Figure 4), we suggest that the one-plume structure may only be responsible for <10% of the geoid in the Tharsis rise (Figures 8b and 8c). The major part of the geoid must be produced from other processes including the surface loading [e.g., *Solomon and Head*, 1982; *Banerdt and Golombek*, 2000; *Phillips et al.*, 2001].

[41] The overestimation by *Harder* [2000] results from an inadequate loading formulation (i.e., instantaneous viscous flow or IVF) that was used to determine the geoid in his models. The IVF formulation seeks steady state responses of surface topography and geoid that cannot be actually achieved when a lithosphere is present (Figure 2). Our more realistic viscoelastic formulation suggests that depending on lithospheric thickness only part of the steady state response of surface topography from the IVF model is observationally relevant. Since the geoid is very sensitive to the surface topography, the reduced response of surface topography has significant implications for the geoid from the IVF formulation (Figure 4).

[42] There are a number of reasons as to why the one-plume structure is inefficient in generating long-wavelength geoid anomalies. Long-wavelength (i.e., degrees 2–4) structures from an upwelling plume are confined to a 200–300 km depth range below the lithosphere and they are generated as hot fluids from the plume spread out below the lithosphere (Figure 7). This depth range is controlled by the thickness of thermal boundary layer. Within this depth range the geoid kernel is nearly zero and the ratio of geoid to topography is also small (Figures 4c and 4d). To reduce elastic thickness does not help produce the geoid, because the long-wavelength structures from the plume are always confined to a layer below the lithosphere in which the geoid kernel is very small (Figure 5b). In fact, in *Harder and Christensen* [1996] with 100 km thick lithosphere, the geoid above the plume is only ~10% of the observed. The increased geoid of *Harder* [2000] is partially caused by the increased lithospheric thickness of 220 km that pushes long-wavelength structures to a greater depth and produces larger geoid anomalies and GTR when the IVF formulation is used to determine the geoid (Figure 5e).

[43] How much could the one-plume structure contribute to the elevated Tharsis topography? The answer depends on the strength of the plume below the Tharsis. It is possible that the plume that may have been responsible for the formation of volcanic construction of the Tharsis rise during the late Noachian has since diminished in its strength such that the plume no longer produces significant uplift. In this scenario, both the elevated topography and geoid in the Tharsis rise should be explained as the loading of volcanic construction on the lithosphere, as previous studies have suggested [e.g., *Solomon and Head*, 1982; *Banerdt and Golombek*, 2000; *Phillips et al.*, 2001].

[44] On the other hand, if a plume like that in Figure 7a exists below the Tharsis rise, the plume may contribute significantly to the elevated Tharsis topography. The plume with its long-wavelength components at shallow depths may produce significant uplift, although its geoid contribution may be very limited (Figures 4a and 4c). The uplift predicted from the viscoelastic loading formulation is only ~20% smaller than that from the IVF formulation (Figure 8a). However, if a significant fraction of the Tharsis topography is dynamically supported by the plume that does not generate much geoid anomalies, this suggests that the Tharsis geoid needs to be explained by surface loads with significantly smaller amount of mass anomalies than the previous surface loading models have assumed. A significantly larger elastic thickness may be needed to generate the Tharsis geoid anomalies with smaller amount of mass anomalies.

[45] One potential way to resolve this issue on how much a plume may contribute to the elevated Tharsis topography is to carefully infer the elastic thickness for surface loads with similar tectonic age but shorter wavelengths than those for the Tharsis rise [*Zuber et al.*, 2000; *McGovern et al.*, 2000; *Arkani-Hamed*, 2000]. With their short wavelengths, the topography and gravity anomalies of surface loads should not be affected by the plume. If the inferred elastic thickness from the short wavelength loads is significantly larger than 150 km that was inferred for the Tharsis rise with models that did not consider the internal loads [e.g., *Zuber et al.*, 2000; *McGovern et al.*, 2000], it is likely that some of the elevated Tharsis topography is supported by the plume and that the actual elastic thickness for the Tharsis rise is larger than the 150 km. If the inferred elastic thickness is similar for loads with different wavelengths, we may conclude that the plume's contribution to the Tharsis topography is minimal.

5. Conclusions

[46] 1) The one-plume structure suggested by *Harder and Christensen* [1996] and *Harder* [2000] if currently existing below the Tharsis rise may only be responsible for a small fraction (e.g., <10%) of the geoid anomalies in the Tharsis rise. This is because the long-wavelength components of the plume structure are confined to a ~300-km thick layer below the lithosphere with which the geoid response is minimal. This implies that the major part of the geoid needs to be explained by other processes including surface loading of volcanic construction on lithosphere.

[47] 2) The plume structure is effective in producing uplifts. However, because the plume does not produce much geoid anomalies, if the elevated Tharsis topography is partly supported by a plume below the Tharsis rise, this implies that in order to explain the geoid anomalies the Tharsis lithosphere needs to be significantly thicker than ~150 km that was inferred from models that did not consider internal loads. More studies are needed to constrain the possible contribution from the mantle buoyancy to the elevated Tharsis topography.

[48] 3) We have demonstrated that the thin elastic shell [e.g., *Turcotte et al.*, 1981] and instantaneous viscous flow (IVF) [e.g., *Hager and Richards*, 1989; *Harder*, 2000] loading formulations are the special cases of a viscoelastic loading formulation. Only a fraction of the steady state response from the IVF formulation is observationally relevant, depending on lithospheric thickness. However, the viscoelastic responses may be simulated by combining the IVF and thin elastic shell formulations under certain conditions.

[49] **Acknowledgments.** This study was partly motivated by discussions in the Tharsis workshop that was held in Keystone of Colorado in October of 2000. The author would like to thank M. Zuber, R. J. Phillips and W. S. Kiefer for helpful discussions and O. Aharonson and an anonymous reviewer for their careful reviews. This research is supported by a NASA grant (NAG5-11224).

References

Anderson, R. C., J. M. Dohm, M. P. Golombek, A. F. C. Haldemann, B. J. Franklin, K. L. Tanaka, J. Lias, and B. Peer, Primary centers and secondary concentrations of tectonic activity through time in the western hemisphere of Mars, *J. Geophys. Res.*, *106*, 20,563–20,585, 2001.

Arkani-Hamed, J., Strength of Martian lithosphere beneath large volcanoes, *J. Geophys. Res.*, *105*, 26,713–26,732, 2000.

Banerdt, W. B., and M. P. Golombek, Tectonics of the Tharsis region of Mars: Insights from MGS topography and gravity, *Proc. Lunar Planet. Sci. Conf. 31st*, abstract 2038, 2000.

Banerdt, W. B., M. P. Golombek, and K. L. Tanaka, Stress and tectonics on Mars, in *Mars*, edited by H. H. Kieffer et al., 249–297, Univ. Ariz. Press, Tucson, 1992.

Breuer, D., D. A. Yuen, T. Spohn, and S. Zhang, Three-dimensional models of Martian mantle convection with phase transitions, *Geophys. Res. Lett.*, *25*, 229–232, 1998.

Brotchie, J. F., and R. Silvester, On crustal flexure, *J. Geophys. Res.*, *74*, 5240–5252, 1969.

Cathles, L. M., *The Viscosity of the Earth's Mantle*, 386 pp., Princeton Univ. Press, Princeton, N.J., 1975.

Christensen, U. R., and D. A. Yuen, Layered convection induced by phase changes, *J. Geophys. Res.*, *90*, 10,291–10,300, 1985.

Grimm, R. E., and S. C. Solomon, Viscous relaxation of impact crater relief on Venus: Constraints on crustal thickness and thermal gradient, *J. Geophys. Res.*, *93*, 11,911–11,929, 1988.

Hager, B. H., and M. A. Richards, Long-wavelength variations in Earth's geoid: Physical models and dynamical implications, *Philos. Trans. R. Soc. London, Ser. A*, *328*, 309–327, 1989.

Han, D., and J. Wahr, The viscoelastic relaxation of a realistically stratified Earth and a further analysis of post-glacial rebound, *Geophys. J. Int.*, *120*, 287–311, 1995.

Harder, H., Mantle convection and the dynamic geoid of Mars, *Geophys. Res. Lett.*, *27*, 301–304, 2000.

Harder, H., and U. Christensen, A one-plume model of Martian mantle convection, *Nature*, *380*, 507–509, 1996.

Hartmann, W. K., Martian cratering, 4, Mariner 9 initial analysis of cratering chronology, *J. Geophys. Res.*, *78*, 4096–4116, 1973.

Kellogg, L., and S. D. King, Effect of mantle plumes on the growth of D" by reaction between the core and mantle, *Geophys. Res. Lett.*, *20*, 379–382, 1993.

Kiefer, W. S., and B. H. Hager, The role of mantle convection in the origin of the Tharsis and Elysium provinces of Mars (abstract), in *Early Tectonic and Volcanic Evolution of Mars*, *LPI Tech. Rep. 89–04*, pp. 48–50, Lunar and Planet. Inst., Houston, Tex., 1989.

Kiefer, W. S., B. G. Bills, and R. S. Nerem, An inversion of gravity and topography for mantle and crustal structure on Mars, *J. Geophys. Res.*, *101*, 9239–9252, 1996.

McGovern, P. J., et al., Localized gravity/topography admittance on Mars, *Proc. Lunar Planet. Sci Conf. 31st*, abstract 1792, 2000.

Mege, D., and P. Masson, A plume tectonics model for the Tharsis province, Mars, *Planet. Space Sci.*, *44*, 1499–1546, 1996.

Peltier, W. R., Glacial isostatic adjustment, II, The inverse problem, *Geophys. J. R. Astron. Soc.*, *46*, 605–646, 1976.

Phillips, R. J., M. T. Zuber, S. C. Solomon, M. P. Golombek, B. M. Jakosky, W. B. Banerdt, R. M. E. Williams, B. M. Hynek, O. Aharonson, and S. A. Hauck II, Ancient geodynamics and global-scale hydrology on Mars, *Science*, *291*, 2587–2591, 2001.

Smith, D. E., et al., The gravity field of Mars: Results from Mars Global Surveyor, *Science*, *286*, 94–97, 1999a.

Smith, D. E., et al., The global topography of Mars and implications for surface evolution, *Science*, *284*, 1495–1503, 1999b.

Solomon, S. C., and J. W. Head, Evolution of the Tharsis province of Mars: The importance of heterogeneous lithospheric thickness and volcanic construct, *J. Geophys. Res.*, *87*, 9755–9774, 1982.

Solomon, S. C., and J. W. Head, Heterogeneities in the thickness of the elastic thickness of Mars: Constraints on heat flow and internal dynamics, *J. Geophys. Res.*, *95*, 11,073–11,083, 1990.

Tanaka, K. L., D. H. Scott, and R. Greeley, Global stratigraphy, in *Mars*, edited by H. H. Kieffer et al., pp. 345–382, Univ. of Ariz. Press, Tucson, 1992.

Turcotte, D. L., and G. Schubert, *Geodynamics*, John Wiley, New York, 1982.

Turcotte, D. L., R. J. Willemann, W. F. Haxby, and J. Norberry, Role of membrane stresses in the support of planetary topography, *J. Geophys. Res.*, *86*, 3951–3959, 1981.

Willemann, R. J., and D. L. Turcotte, The role of lithospheric stress in the support of the Tharsis rise, *J. Geophys. Res.*, *87*, 9793–9801, 1982.

Zhong, S., Dynamics of crustal compensation and its influences on crustal isostasy, *J. Geophys. Res.*, *102*, 15,287–15,299, 1997.

Zhong, S., and G. F. Davies, Effects of plate and slab viscosities on the geoid, *Earth Planet. Sci. Lett.*, *170*, 487–496, 1999.

Zhong, S., and M. Gurnis, The role of plates and temperature-dependent viscosity in phase change dynamics, *J. Geophys. Res.*, *99*, 15,903–15,917, 1994.

Zhong, S., and M. T. Zuber, Long-wavelength topographic relaxation for self-gravitating planets and its implications to the compensation of lunar basins, *J. Geophys. Res.*, *105*, 4153–4164, 2000.

Zhong, S., and M. T. Zuber, Degree-1 mantle convection and the crustal dichotomy on Mars, *Earth Planet. Sci. Lett.*, *189*, 75–84, 2001.

Zhong, S., M. Gurnis, and L. Moresi, Free surface formulation of mantle convection, part 1, Basic theory and implication to plumes, *Geophys. J. Int.*, *127*, 708–718, 1996.

Zuber, M. T., et al., Internal structure and early thermal evolution of Mars from Mars Global Surveyor topography and gravity, *Science*, *287*, 1788–1793, 2000.

S. Zhong, Department of Physics, University of Colorado at Boulder, Campus Box 390, Boulder, CO 80309-0390, USA. (szhong@spice.colorado.edu)